Shape Memory Polymer Composite Booms with Applications in Reel-Type Solar Arrays

Hong Xiao[1*] , Sijie Wu[1,2], Dongdong Xie[1], Hongwei Guo[1], Li Ma[3], Yuxuan Wei[3] and Rongqiang Liu[1]

Abstract

Solar arrays are the primary energy source for spacecraft. Although traditional rigid solar arrays improve power supply, the quality increases proportionally. Hence, it is difficult to satisfy the requirements of high-power and low-cost space applications. In this study, a shape-memory polymer composite (SMPC) boom was designed, fabricated, and characterized for flexible reel-type solar arrays. The SMPC boom was fabricated from a smart material, a shape-memory polymer composite, whose mechanical properties were tested. Additionally, a mathematical model of the bending stiffness of the SMPC boom was developed, and the bending and buckling behaviors of the boom were further analyzed using the ABAQUS software. An SMPC boom was fabricated to demonstrate its shape memory characteristics, and the driving force of the booms with varying geometric parameters was investigated. We also designed and manufactured a reel-type solar array based on an SMPC boom and verified its self-deployment capability. The results indicated that the SMPC boom can be used as a deployable unit to roll out flexible solar arrays.

Keywords Shape memory polymer composite, Reel-type solar array, Deployable boom, Bending behavior

1 Introduction

A solar array is a crucial component for spacecraft energy supply, and it ensures that a spacecraft can function normally [1]. In recent years, human space activities have increased, and the demand for large-scale solar arrays with high power and low cost has grown accordingly. Traditional rigid arrays not only increase the area of the array, but also proportionally increase its mass, which leads to an increase in launch costs. Furthermore, this affects the mechanical properties of the spacecraft. Conversely, flexible solar arrays use triple-junction (3 J) solar cells integrated on a flex array blanket, which exhibit the characteristics of light weight and simple structure with high storage ratio [2, 3]. Flexible solar arrays have become more attractive owing to their lower specific packing

volume (W/m^3) and high specific power (W/kg). The most common forms of flexible solar arrays are Z-folded and Z-reeled. The latter can be stowed in a cylindrical volume for more efficient space utilization. It can also be partially deployed to adapt to varying conditions.

The reel-type solar array was first used in the Hubble space telescope (HST) as a flexible rolled-up solar array (FRUSA) [4, 5]. As shown in Figure 1, FRUSA solar array primarily consists of flexible solar cell blankets, a stowage drum, spreader bars, and deployable booms. The booms are fabricated from thin stainless-steel strips shaped into circular cross-sections that are flattened and stored on cassettes within the mechanism. During deployment, the booms are driven by a motor, and then the blanket is pulled from the drum via spreader bars to deploy the solar array.

Roll-out solar array (ROSA) was conceived and developed by deployable space systems, Inc. (DSS), and it was successfully validated in orbit in 2017 [3, 6–8]. The configuration of ROSA solar array is shown in Figure 2, which mainly includes a root structure, an IMBA blanket, a mandrel, and two deployable composite booms. When

*Correspondence:
Hong Xiao
xiaohong@hit.edu.cn
[1] State Key Laboratory of Robotics and System, Harbin Institute of Technology, Harbin 150006, China
[2] Yinhe Hangtian Internet Technology Co., Ltd., Beijing 100192, China
[3] China Academy of Space Technology, Beijing 100098, China

Xiao *et al. Chinese Journal of Mechanical Engineering*   (2023) 36:67
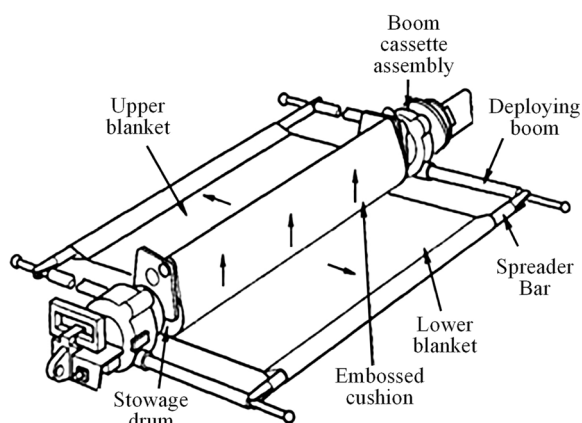
Page 2 of 13

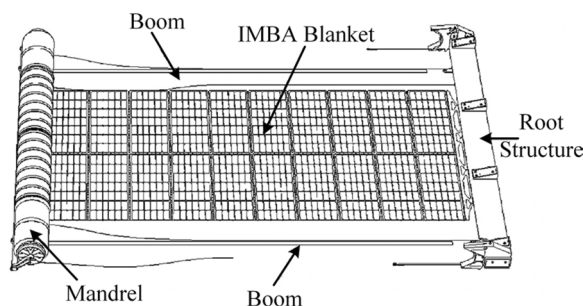**Figure 1** FRUSA solar array

Figure 2 ROSA solar array

configured for launch, ROSA solar array is stowed into a compact cylindrical volume, and the wing is rolled out by using booms with stored strain energy without requiring complex, heavy, and costly motors, or other complicated deployment mechanisms.

It can be observed from FRUSA and ROSA solar arrays that the deployable booms play an important role in the deployment and retraction of the solar arrays. The thin-walled tubular deployable boom mainly includes a storable tubular extendable member (STEM) and collapsible tubular mast (CTM), which utilize the elastic deformation of thin-walled shells or motor drives to realize deployment. Beryllium alloys, molybdenum, tungsten, and carbon fiber reinforced composites (CFRP) are commonly used as extendable arms [9]. With continuous development of smart materials, space deployment technologies based on thermally induced shape memory polymers (SMPs) and their composites (SMPCs) have gained significant attention in recent years [10–12]. SMP and SMPC can respond to specific conditions and remember their original shape. Hence, they exhibit great potential for application in space-deployable structures [13–15]. Furthermore, SMPs exhibit strong deformability and a good shape memory effect, and are usually composed

of soft segment elements and hard segment elements, which work together to realize the shape memory effect [16]. Compared with SMPC, SMP has less recovery driving force and poor mechanical properties. Hence, it is necessary to add particulates or fibers as reinforcements to prepare composite materials to solve this problem. Yu et al. [17] added modified glass beads to shape memory polymers to improve the tensile strength of the material. Furthermore, the material exhibits excellent photothermal properties, which can reach the switching temperature in a short time. Leng et al. [18] enhanced the conductivity of SMP by adding Ni to the matrix. Liu et al. [19] added various short and continuous carbon fibers into a neat shape memory epoxy matrix to realize superior mechanical properties such as tensile strength and bending stiffness. Applications of SMP and SMPC in the aerospace field mainly include hinges, locking mechanisms, deployable trusses, and flexible solar panels. The CTD [20] examined a shape memory polymer resin and applied it to the hinge of the TacSat-2 satellite, which is approximately 100 mm long, and thermal protection is realized through a thermal protection film. Zhao et al. [21] proposed a separation and locking device composed of a metal structure with internal dents and an external SMPC tube and tested its bearing capacity via tensile tests. Li et al. [22, 23] proposed a deformable load-bearing deployable truss structure that provides a driving force for support via SMPC arc laminates and can be used as the driving mechanism and supporting structure. By applying the shape memory of SMPC to thin-walled tubular space extendable arms, the complex hinges and control assembly can be significantly reduced, resulting in a highly compact and lightweight design.

Considering the advantages of flexible solar arrays and SMPC, a new scheme of flexible solar arrays based on SMPC booms is presented in this study. As opposed to existing flexible solar arrays, this solar array uses the shape-memory characteristics of SMPC rather than elastic strain energy or motor driving to drive its deployment, which is a major difference from existing studies. Compared with the traditional rigid-hinge solar array, it exhibits the advantages of controllable deployment speed and no impact at the end of deployment. The primary objectives of this study include: (1) Testing the mechanical properties of SMPC; (2) detailed design, analysis, and verification of the SMPC boom; and (3) mechanical design and demonstration testing of the prototype flexible reel-type solar array.

2 Mechanical Properties of SMPC

2.1 Mechanical Properties Testing

Shape memory polymers (SMPs) and their composites (SMPCs) are smart materials that can respond to specific
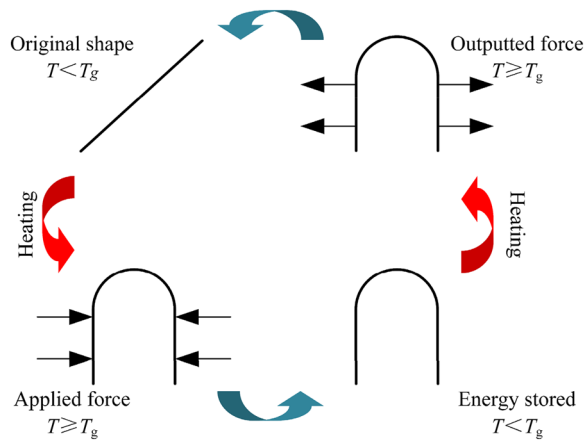
Figure 3 Typical cycle for thermally induced shape memory effect

external stimuli (such as heat and light) and remember their original shapes [10–15]. Figure 3 illustrates a typical cycle of the thermally induced shape memory effect. First, the SMPC was deformed into its original shape. Then, its temperature was raised above the glass transition temperature (T_g). Subsequently, the SMPC was deformed by an external force. Afterwards, the SMPC was cooled below T_g and the constraint was removed. Finally, the SMPC was heated above T_g to induce the shape-memory effect. Owing to its entropy elasticity, SMPC recovers its original shape.

In this study, a new type of carbon-fiber-reinforced epoxy-based SMPC was developed that uses epoxy-SMP resin as the matrix material. The composite was reinforced with T300 1 K fiber plain-weave fabric and fabricated using an autoclave molding technique. Each layer of the laminate of the SMPC specimen was stacked by completely consistent single-layer plates. Therefore, the SMPC laminates can be considered as single-layer plates with a specific thickness [24]. Considering the utilization of material parameters in subsequent studies, we specified a 45° angle with the fiber orientation as the principal axis of the material, as shown in Figure 4 ($\theta = 45°$). The SMPC material properties were obtained using standard test methods for polymer matrix composite materials, including tensile properties (ASTM D3039 [25]), shear properties (ASTM D5379 [26]), and in-plane properties (ASTM D3518 [27]). The measurement results are listed in Table 1.

Further investigation of the thermomechanical properties of the SMPC was performed using dynamic thermomechanical analysis (DMA) via DMA Q800. A three-point mode was applied to specimens of dimensions 50 mm × 10 mm × 2 mm and a gauge length of 30 mm. The scanning range of temperature was − 100 to 150 °C at a heating rate of 1 °C/min, and a frequency
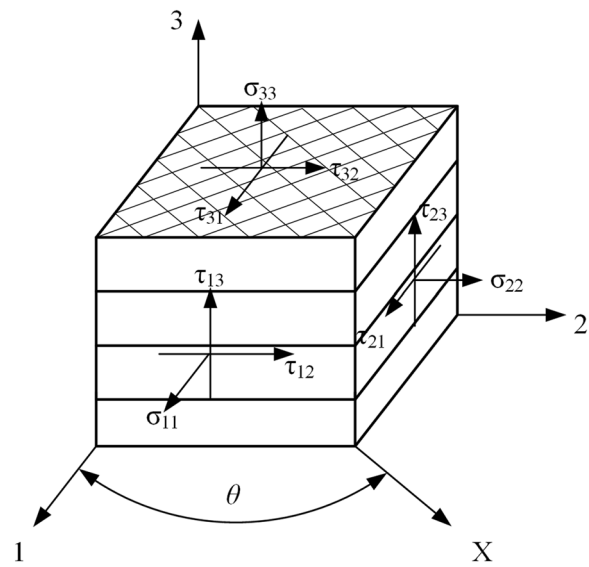
Figure 4 Material coordinate system of SMPC

Table 1 Primary mechanical parameters of SMPC

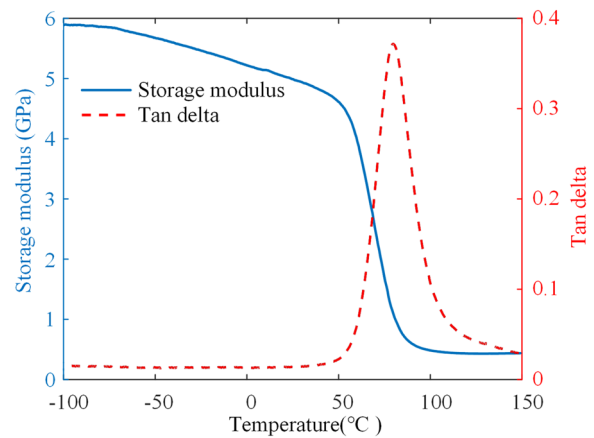| Parameters	Value
Longitudinal modulus $E_1 = E_2$ (GPa)	8.76
In-plane shear modulus G_{12} (GPa)	2.26
Out-plane shear modulus $G_{13} = G_{23}$ (GPa)	1.39
Longitudinal Poisson's ratio v_{12}	0.90
Transverse Poisson's ratio $v_{13} = v_{23}$	0.22

Figure 5 SMPC DMA temperature spectrum

of 1 Hz. The test results are shown in Figure 5. As shown in the figure, the peak value of the tangent delta is located at 80 °C, which is defined as the glass transition temperature (T_g). The SMPC maintains a high storage modulus in the glass state in the range of − 100
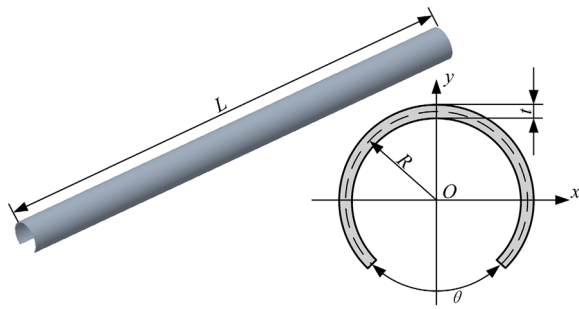
Figure 6 Diagram of the SMPC boom

to 50 °C, which is approximately 5 GPa at room temperature (25 °C). In the glass transition region, namely 50–100 °C, the storage modulus decreases significantly owing to the phase transition. When the temperature exceeded 100 °C, the SMPC matrix turned into a viscoelastic state, and the storage modulus was approximately 0.4 GPa.

2.2 Stiffness Matrix of SMPC Laminate

The characteristics of SMPC were analyzed based on the macromechanics of the composites [12]. Under in-plane stress, the stress–strain relationship in the principal direction of a single-layer SMPC can be simplified as follows:

$$\begin{bmatrix} \sigma_1 \\ \sigma_2 \\ \tau_{12} \end{bmatrix} = \begin{bmatrix} Q_{11} & Q_{12} & 0 \\ Q_{12} & Q_{22} & 0 \\ 0 & 0 & Q_{66} \end{bmatrix} \begin{bmatrix} \varepsilon_1 \\ \varepsilon_2 \\ \gamma_{12} \end{bmatrix} = \boldsymbol{Q}\boldsymbol{\varepsilon}, \quad (1)$$

where $\boldsymbol{Q}$ denotes the two-dimensional stiffness matrix of the composite, ε_1 and ε_2 are the positive strains in direction 1 and direction 2, γ_{12} is the shear strain and Q_{ij} is expressed by engineering the elastic constant as follows:

$$\begin{cases} Q_{11} = \frac{E_1}{1-\mu_{12}\mu_{21}}, Q_{22} = \frac{E_2}{1-\mu_{12}\mu_{21}}, \\ Q_{12} = \frac{\mu_{12}E_1}{1-\mu_{12}\mu_{21}} = \frac{\mu_{12}E_2}{1-\mu_{12}\mu_{21}}, Q_{66} = G_{12}. \end{cases} \quad (2)$$

Furthermore, based on the classical laminate theory (CLT), the constitutive relationship of composite laminates is as follows:
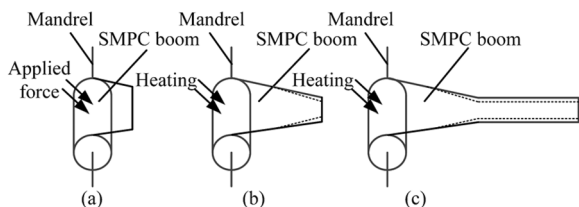

Figure 7 Principle of the deployment of the SMPC boom: **a** Fully stowed, **b** Partially deployed, **c** Fully deployed

$$\begin{bmatrix} N_x \\ N_y \\ N_{xy} \\ M_x \\ M_y \\ M_{xy} \end{bmatrix} = \begin{bmatrix} A_{11} & A_{12} & A_{16} & B_{11} & B_{12} & B_{16} \\ A_{12} & A_{22} & A_{26} & B_{12} & B_{22} & B_{26} \\ A_{16} & A_{26} & A_{66} & B_{16} & B_{26} & B_{66} \\ B_{11} & B_{12} & B_{16} & D_{11} & D_{12} & D_{16} \\ B_{12} & B_{22} & B_{26} & D_{12} & D_{22} & D_{26} \\ B_{16} & B_{26} & B_{66} & D_{16} & D_{26} & D_{66} \end{bmatrix} \begin{bmatrix} \varepsilon_x^0 \\ \varepsilon_y^0 \\ \gamma_{xy}^0 \\ k_x \\ k_y \\ k_{xy} \end{bmatrix}. \quad (3)$$

As mentioned previously, the SMPC laminate can be regarded as a special orthotropic single-layer plate with a specified thickness (t=1 mm). The stiffness of the laminate is as follows:

$$\begin{cases} A_{11} = Q_{11}t, & D_{11} = \frac{Q_{11}}{12}t^3, \\ A_{12} = Q_{12}t, & D_{12} = \frac{Q_{12}}{12}t^3, \\ A_{22} = Q_{22}t, & B_{ij} \equiv 0, \quad D_{22} = \frac{Q_{22}}{12}t^3, \\ A_{16} = A_{26} = 0, & D_{16} = D_{26} = 0, \\ A_{66} = Q_{66}t, & D_{66} = \frac{Q_{66}}{12}t^3. \end{cases} \quad (4)$$

By substituting the values, the stiffness matrix of SMPC laminate can be obtained as follows:

$$\boldsymbol{A} = \begin{bmatrix} 46.1 & 41.5 & 0 \\ 41.5 & 46.1 & 0 \\ 0 & 0 & 2.26 \end{bmatrix} \times 10^6 \text{ N} \cdot \text{m}^{-1},$$

$$\boldsymbol{B} = 0 \text{ N},$$

$$\boldsymbol{D} = \begin{bmatrix} 3.84 & 3.46 & 0 \\ 3.46 & 3.84 & 0 \\ 0 & 0 & 0.19 \end{bmatrix} \text{ N} \cdot \text{m}.$$

3 Mechanical Performances of the SMPC Boom
3.1 Working Principle

In this section, a thin-walled boom made of SMPC was developed for a reel-type solar array. The SMPC boom is a storable tubular extendable member, whose cross-sectional shape is an open cylindrical shell. As illustrated in Figure 6, the design dimensions of the SMPC boom include length L, radius of the cross-sectional neutral surface R, thickness t, and opening angle of the circular ring θ.
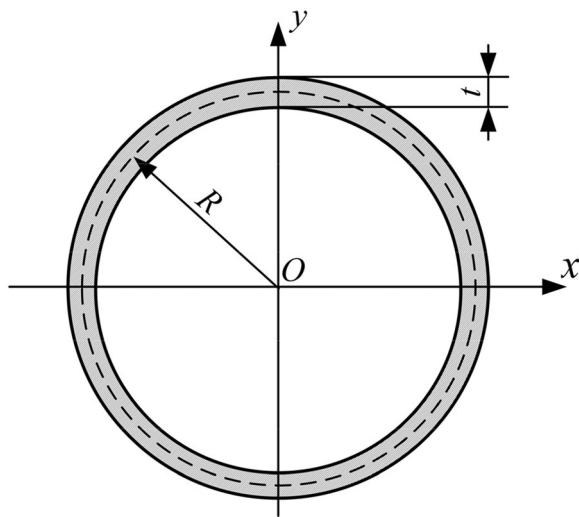
Figure 8 Cross-section of laminated tubes

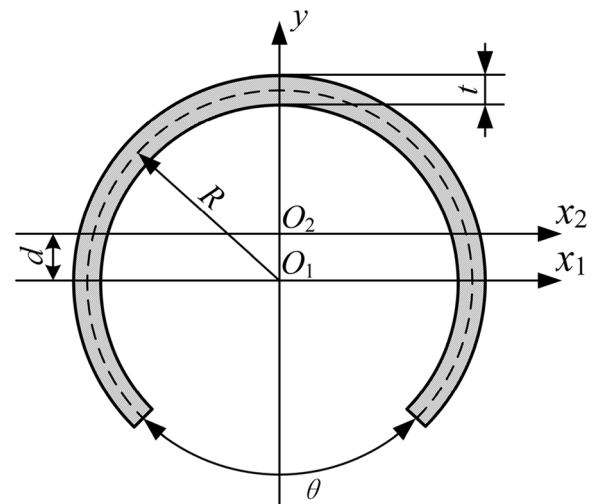**Figure 9** Cross-section of SMPC booms

The SMPC boom is initially in an unfolded state, and the structure softens as it is heated above T_{g}. At this time, an external force is applied to flatten and fix the root of the SMPC boom on the mandrel and then roll the boom into the mandrel, as shown in Figure 7(a). The coiled section of the SMPC boom is heated, and the boom slowly recovers to its original shape because of the shape memory characteristics of the SMPC, as shown in Figure 7(b). Furthermore, the fully deployed state of the SMPC boom is shown in Figure 7(c).

3.2 Bending Behavior

The SMPC boom must be cooled and hardened after it is fully deployed and rolls out the solar blanket. At this time, the bending stiffness of the SMPC boom is significantly improved. The bending stiffness of the SMPC boom indicates its ability to resist external interference and directly influences the deployed frequency of the solar array. Therefore, it is necessary to conduct pertinent research on the bending stiffness of SMPC boom. The mathematical model of the bending stiffness of the SMPC boom was developed by considering: (1) the bending stiffness of a thin-walled composite tube with a circular cross-section; and (2) the equivalent bending stiffness of the SMPC boom (opening circular ring cross-section) was derived using the moment of inertia of the material mechanics.

In Ref. [28], a detailed derivation of the equivalent bending stiffness of a composite tube with a circular cross-section was presented. Based on the non-classical composite beam theory, Shadmehri et al. comprehensively considered the effects of transverse shear deformation, non-uniform twist, and warping inhibition of composite materials and calculated the analytical solution of the bending stiffness of composite tubes for any arbitrary cross-sectional shape as follows:

$$
\begin{aligned}
[EI] = \pi R \Big\{ R^2 \Big[&\Big(A_{22} - \frac{A_{12}^2}{A_{11}}\Big)\Big(A_{66} - \frac{A_{16}^2}{A_{11}}\Big) + A_{44}\Big(A_{22} - \frac{A_{12}^2}{A_{11}}\Big) - \Big(A_{26} - \\
&\frac{A_{12}A_{16}}{A_{11}}\Big)^2 \Big] + 2R\Big[\Big(B_{22} - \frac{A_{12}B_{12}}{A_{11}}\Big)\Big(A_{66} - \frac{A_{16}^2}{A_{11}}\Big) + A_{44}\Big(B_{22} - \frac{A_{12}B_{12}}{A_{11}}\Big) \\
&- \Big(A_{26} - \frac{A_{16}B_{12}}{A_{11}}\Big)\Big(B_{26} - \frac{A_{16}B_{12}}{A_{11}}\Big)\Big] + \Big[\Big(D_{22} - \frac{B_{12}^2}{A_{11}}\Big)\Big(A_{66} - \frac{A_{16}^2}{A_{11}}\Big) + \\
&A_{44}\Big(D_{22} - \frac{B_{12}^2}{A_{11}}\Big) - \Big(B_{26} - \frac{A_{16}B_{12}}{A_{11}}\Big)^2 \Big] \Big\} \Big/ \Big(A_{66} - \frac{A_{16}^2}{A_{11}} + A_{44}\Big).
\end{aligned}
\tag{5}
$$

By substituting Eq. (4) into Eq. (5), the equivalent bending stiffness of the SMPC laminated tube developed in this study is as follows:

$$[EI] = \pi R \left[R^2 \left(A_{22} - \frac{A_{12}^2}{A_{11}} \right) + D_{22} \right]. \tag{6}$$

By substituting Eq. (2) and Eq. (4) into Eq. (6) and degrading the material properties, the equivalent bending stiffness can be expressed as follows:

$$[EI] = \pi R^3 t \tilde{A} + \pi R t^3 \tilde{D}, \tag{7}$$

where $\tilde{A}$ and $\tilde{D}$ are related to the engineering constants of the SMPC. It can be observed from Eq. (7) that when the material and stacking directions are fixed ($\tilde{A}$, $\tilde{D}$ are constant), the equivalent bending stiffness of the SMPC laminated tube is dependent on its geometric parameters, such as radius R, and thickness t.

According to the equivalent bending stiffness of the laminated tube (the cross-section is a closed circular ring, as shown in Figure 8), a theoretical derivation using the moment of inertia was performed to obtain the equivalent bending stiffness of the SMPC boom (the cross-section is an opening circular ring, as shown in Figure 9). In Figure 9, O_1 denotes the center of the opening ring, and the cross-section is symmetric with respect to the y-axis. It is assumed that O_2 is the centroid of the cross-section, $O_1O_2 = d$, and that x_2-axis is perpendicular to the y-axis through the centroid point; that is, x_2-axis is the centroid principal axis of inertia.

The moment of inertia of the area (Figure 9) with respect to x_1-axis is calculated as follows:

$$I_{x1} = \iint_A y^2 \, \mathrm{d}A = 2 \int_{R-\frac{t}{2}}^{R+\frac{t}{2}} R\mathrm{d}R \int_{\theta_1-\frac{\pi}{2}}^{\frac{\pi}{2}} R^2 \sin^2 \theta \mathrm{d}\theta. \tag{8}$$

As $t \ll R$, the quadratic and higher functions of t can be ignored. Hence, Eq. (8) can be simplified as follows:

$$I_{x1} = R^3 t \left[\pi - \theta_1 - \frac{\sin 2\theta_1}{2} \right], \tag{9}$$

where θ denotes the opening angle, $\theta = 2\theta_1$. According to the first moment of the area, the centroidal distance in the y-direction can be expressed as follows:

$$d = \frac{\iint_A y \mathrm{d}A}{A} = \frac{2 \int_{R-\frac{t}{2}}^{R+\frac{t}{2}} R\mathrm{d}R \int_{\theta_1-\frac{\pi}{2}}^{\frac{\pi}{2}} R \sin \theta \mathrm{d}\theta}{A}, \tag{10}$$

where S_{x1} denotes the first moment about the x-axis, A denotes the area of the opening ring, $A = (\pi - \theta_1)[R^2 - (R-t)^2]$. In accordance with the
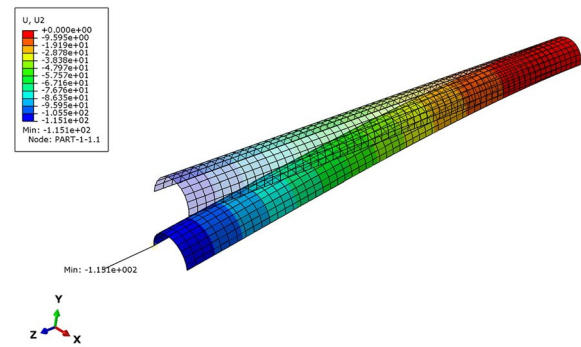

Figure 10 Displacement contour of the SMPC boom under radial load

Table 2 Analysis of bending stiffness for the SMPC boom

θ (°)	R (mm)	t (mm)	Theoretical value (N·m²)	Simulation value (N·m²)	Difference (%)
120	20	1.2	79.61	77.66	2.45
120	25	1.0	129.46	125.55	3.02
180	15	1.2	10.59	10.00	5.57
180	25	0.8	32.58	31.27	4.02
240	15	1.0	1.42	1.35	4.93
240	20	0.8	2.68	2.61	2.61

parallel-axis theorem, the moment of inertia with respect to the x_2-axis can calculated as follows:

$$I_{x2} = I_{x1} - d^2 A = R^3 t \left[\pi - \theta_1 - \frac{\sin 2\theta_1}{2} - \frac{2 \sin^2 \theta_1}{\pi - \theta_1} \right]. \tag{11}$$

When the cross-section is a closed ring (Figure 8), $\theta = 0$, and the moment of inertia is as follows:

$$I_x = \pi R^3 t. \tag{12}$$

Based on Eqs. (11) and (12), the ratio of the bending stiffness of the open circular tubes to that of the closed circular tubes is as follows:

$$\rho = \frac{I_{x2}}{I_x} = \frac{\pi - \theta_1 - \frac{\sin 2\theta_1}{2} - \frac{2 \sin^2 \theta_1}{\pi - \theta_1}}{\pi}. \tag{13}$$

Combining Eqs. (7) and (12), the equivalent bending stiffness of the SMPC boom with an arbitrary opening angle can be obtained as follows:

$$\overline{EI} = [EI] \cdot \rho = \left[\pi - \frac{\theta + \sin \theta}{2} - \frac{2(1 - \cos \theta)}{2\pi - \theta} \right] \left(R^3 t \tilde{A} + R t^3 \tilde{D} \right). \tag{14}$$

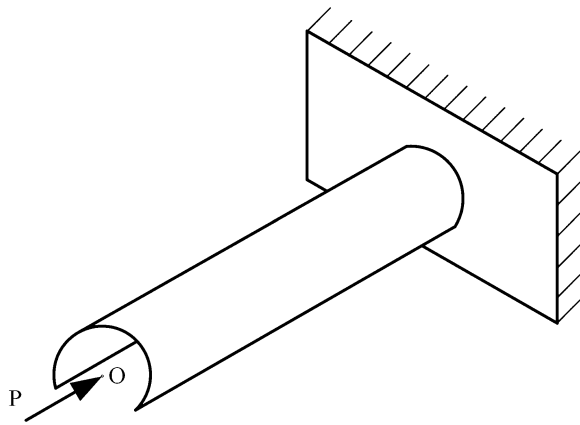To verify the accuracy of Eqs. (14), we used finite element analysis (FEA) with ABAQUS to investigate the

Xiao *et al. Chinese Journal of Mechanical Engineering*   (2023) 36:67

Page 7 of 13

Figure 11 Diagram of the SMPC boom under axial compression

Table 3 Critical loads for the SMPC boom under compression

| θ (°)	R (mm)	t (mm)	Theoretical value (N)	Simulation value (N)	Difference (%)
120	20	1.2	299.40	299.85	− 0.15
120	25	1.0	484.04	487.69	− 0.75
180	15	1.2	38.53	39.94	− 3.66
180	25	0.8	120.54	121.36	− 0.68
240	15	1.0	5.19	5.35	− 3.08
240	20	0.8	10.05	10.01	0.40

equivalent bending stiffness of the SMPC boom. The material parameters of the SMPC boom are listed in Table 1. There are reference points (RP-1 and RP-2) in the two footprints of the finite element model of the SMPC boom, and coupling constraints were established between the reference points and footprints. This can be equivalent to a cantilever beam after the SMPC boom is fully deployed. Therefore, an encastre boundary condition was imposed at RP-2, and a radial load was applied at RP-1. The SMPC boom was meshed with S4R elements (4-node, reduced integration). The displacement contour of the SMPC boom under radial load is shown in Figure 10.

The cantilever beam deflection formula $\omega = Fl^3\big/3EI$ can be used to determine the bending stiffness of an SMPC boom. In this study, six groups of different geometric parameters were analyzed, and the geometric parameters were substituted into Eq. (14) to obtain the theoretical value of the equivalent bending stiffness. The simulation and theoretical values for the SMPC boom are presented in Table 2.
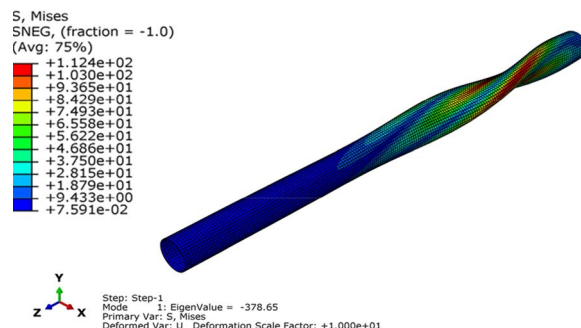
In Table 2, it can be observed that the theoretical and simulation values of the bending stiffness of the SMPC

Table 4 Geometric parameters of torsional buckling of the SMPC boom

Parameter	θ (°)	R (mm)	t (mm)	L (mm)
Value	120	25	1	800
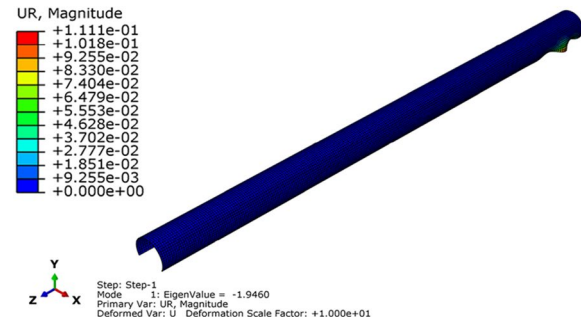
(a)

(b)

Figure 12 Simulation of torsional buckling of SMPC booms with different angles: **a** $\theta = 120°$, **b** $\theta = 0°$

boom differ by less than 6%. Hence, it can be considered that the mathematical model (Eq. (14)) of the equivalent bending stiffness of the SMPC boom is relatively accurate, thereby providing a theoretical basis for structural optimization and engineering applications.

3.3 Buckling Performance

As the core component of the flexible solar array, the SMPC boom must overcome the frictional resistance to roll out the solar-cell blanket. It is also necessary to satisfy the demands of the tension of the solar-cell blanket after it has been fully deployed. The long and slender shape of the SMPC boom can lead to buckling when it is subjected to compression loads (such as frictional resistance and tension of the blanket). Therefore, special

Xiao *et al. Chinese Journal of Mechanical Engineering*   (2023) 36:67

Page 8 of 13

attention must be given to the buckling performance of the SMPC boom.

The SMPC boom can be considered as a cantilever beam with a fixed support at its base and free at its tip, as shown in Figure 11. In this case, the critical load for the SMPC boom is as follows:

$$Pcr = \frac{\pi^2 EI}{4L^2}. \tag{15}$$

Additionally, we developed a finite element model of the SMPC boom in ABAQUS to determine the critical load. In this study, six different geometric parameters of the SMPC boom were simulated and substituted into Eq. (15) for the calculation and verification. The results of the FEA and theoretical calculations for the boom, $L = 800$ mm, are listed in Table 3.

According to Table 3, the critical load for the axial compression of the SMPC boom differs by less than 5% between the simulation and theoretical calculations. Thus, Eq. (15) and the finite element models were mutually verified. The SMPC boom can buckle axially and torsionally, especially for an open thin-walled boom, because the cross-section has a very low torsional stiffness. This in turn leads to easy torsional buckling. Accordingly, a torsional buckling analysis of the SMPC boom is presented in this study based on the axial compression buckling finite element model.

A finite element model of the torsional buckling of the SMPC boom was developed. The geometric parameters of the SMPC boom are presented in Table 4. As shown in Figure 12(a), the eigenvalue of torsional buckling was 1.946 when a torque of 1 N·m was applied to the cantilever end of the SMPC boom, implying that the load of

(a)

(b)

Figure 14 SMPC boom in **a** deployed and **b** stowed states

torsional buckling was 1.946 N·m. Comparatively, FEA of a laminated tube with closed cross-section (i.e., $\theta = 0°$) was also conducted in this study, and the torsional buckling load was 378.65 N·m, nearly 200 times that of the SMPC boom. Consequently, if a thin-walled circular tube is cut at a particular opening angle, the torsional buckling performance is severely compromised.

We further investigated the influence of geometric parameters on the torsional buckling performance of the SMPC boom. The parameters to be examined are set in a certain range, and others are maintained consistently in Table 4, where the thickness, t, ranges from 0.4 mm to 2.0 mm with an intergroup interval of 0.2 mm. Furthermore, the radius of the cross-sectional neutral surface, R, ranged from 10 mm to 50 mm with an intergroup interval of 5 mm; opening angle, θ, ranged from 60° to 220° with an intergroup interval of 20°; and length, L, ranged from 500 mm to 1300 mm with an intergroup interval of 100 mm. Furthermore, ABAQUS was used to calculate the torsional buckling load of the SMPC boom for various geometric parameters. The effects of the geometric
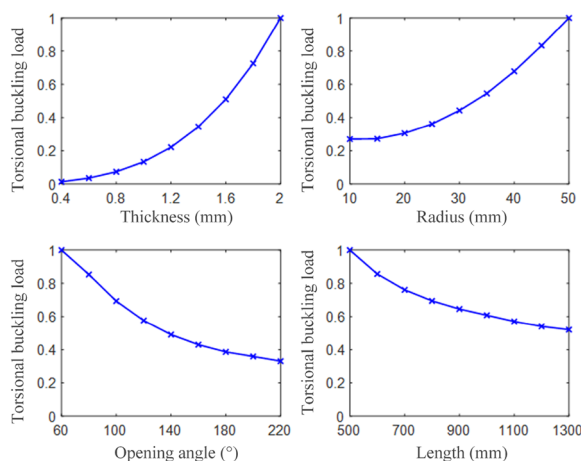

Figure 13 Effects of normalized geometric parameters on torsional buckling of SMPC boom

parameters on the torsional buckling load are illustrated in Figure 13, where the vertical coordinate represents the normalized parameter.

As illustrated in Figure 13, the torsional buckling load of the SMPC boom increased monotonically as the thickness and radius increased, but the load decreased monotonically as the opening angle and length increased. The torsional buckling load of the SMPC boom initially increased slowly as the thickness increased. However, subsequently, it increased rapidly. This implies that when the thickness is low, the torsional buckling load is not significantly affected by the increase in thickness, whereas when the thickness is large, an increase in the thickness has a greater effect. The influence of the radius on the torsional buckling of the SMPC boom is essentially the same as that of the thickness; however, the growth rate of the thickness is more prominent, suggesting that the torsional buckling load of the SMPC boom is more dependent on the thickness. Conversely, as shown in Figure 13, as the opening angle and length increase, the torsional buckling load of the SMPC boom first decreases rapidly and then decreases more gradually. Hence, the effect of the increase in the opening angle and length weakens gradually. Additionally, the torsional buckling load of the SMPC boom was more sensitive to the opening angle.

4 Fabrication and Experimental Test of the SMPC Boom

4.1 Fabrication and Shape Memory Verification

In this study, we fabricated an SMPC boom with a length of 800 mm and demonstrated its shape memory functionality. As shown in Figure 14(a), the SMPC boom is in its initial deployment state. The SMPC boom is heated to a temperature above T_g until it softens. Then, an external force is applied to roll the boom into a mandrel. By maintaining the external force until the boom reaches
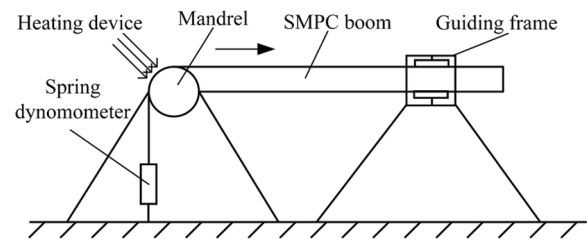

Figure 16 Experimental setup for measuring the driving force of the SMPC boom

room temperature, the SMPC boom can maintain its rolled configuration, as shown in Figure 14(b). Hence, the deployment to stow ratio is 23:1.

An experiment was conducted to investigate the self-deployment behavior of the SMPC boom. Considering the actual operating conditions, we placed the pre-deployment SMPC boom inside a heating chamber and increased the temperature above T_g. Figure 15 illustrates the deployment process of the SMPC boom without external assistance. Based on the experiment, the SMPC boom rolled a distance of approximately 100 mm from the mandrel smoothly within 75 s, demonstrating the shape-memory capability of the SMPC boom. Various deployment velocities can be realized by adjusting the geometric parameters, such as opening angle, thickness, and radius of the SMPC boom.

4.2 Driving Force Testing

Owing to the self-deployment characteristics of the SMPC boom, it is possible to roll out a flexible solar cell blanket without an additional driving motor. When the SMPC boom recovers to its original shape, the force generated is an important indicator of the driving performance of the boom, which directly affects the driving capability of the
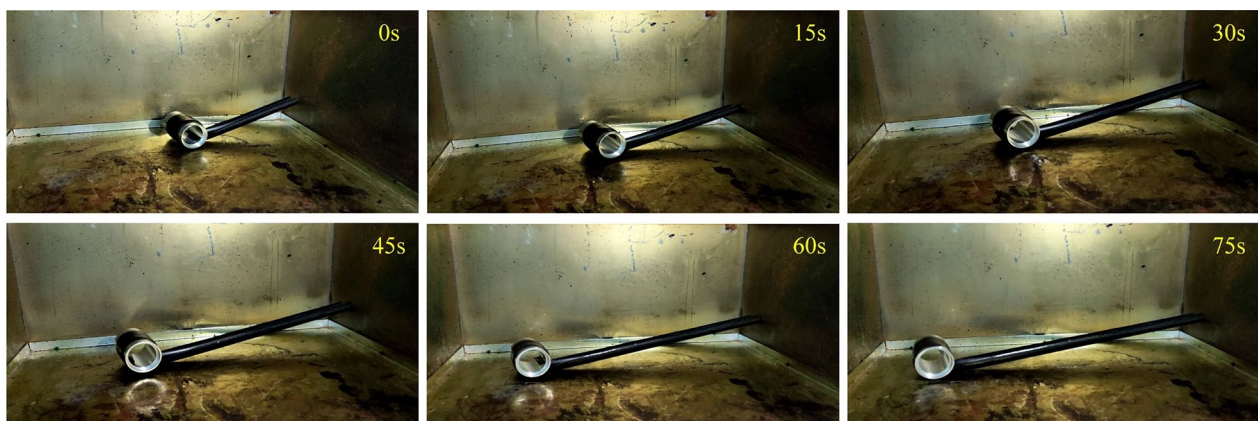

Figure 15 Deployment process of the SMPC boom

Table 5 Orthogonal test results for the driving force of SMPC booms

No.	R (mm)	θ (°)	t (mm)	Driving force (N)
1	9	60	6	0.55
2	9	120	8	0.38
3	9	180	10	0.26
4	9	240	12	0.19
5	12	60	8	1.01
6	12	120	6	0.89
7	12	180	12	0.48
8	12	240	10	0.43
9	15	60	10	1.37
10	15	120	12	1.09
11	15	180	6	1.22
12	15	240	8	0.87
13	18	60	12	2.30
14	18	120	10	2.11
15	18	180	8	1.95
16	18	240	6	1.85

Table 6 Variance analysis of the orthogonal test about the driving force of SMPC booms

Source	SS	df	MS	F	Prominence
R	6.5204	3	2.1735	207	***
θ	0.4880	3	0.1627	15.4952	**
t	0.0278	3	0.0093	0.8857	–
Error	0.0630	6	0.0105	–	–
Total	7.0992	12	–	–	–

deployment mechanism. Figure 16 illustrates the experimental setup for measuring the recovery force (i.e., the driving force). The detailed experimental method is as follows. First, the SMPC boom is reeled along the mandrel and one end of the spring dynamometer is connected to the mandrel while maintaining the other end as fixed. Second, by heating the coiled section of the SMPC boom above T_g, the friction and resistance are overcome (primarily due to the deformation of the spring dynamometer), and thereby, it is deployed solely in the axial direction under the constraint of the guiding frame. Third, as the SMPC boom deploys, the resistance increases gradually until the boom stops unrolling, and at that point, the indication of the spring dynamometer can be considered as the magnitude of the driving force of the boom.

The relationship between the driving force and geometric parameters of SMPC booms was further explored via orthogonal experiments [29]. Based on the analysis and experimental results, three factors were included in the orthogonal matrix: radius R, opening angle $θ$, and thickness t. In each factor, there were four levels as follows: R: 9, 12, 15, 18 mm; $θ$: 60°, 120°, 180°, 240°; and t: 6, 8, 10, 12 mm. Given that there were three experimental factors and four levels for each factor, an orthogonal matrix, denoted as $L_{16}(4^5)$, was selected for the experimental design. The results of the orthogonal tests are presented in Table 5.

Variance analysis was performed to provide a standard for estimating the significance of parameters [29]. The results are listed in Table 6, where SS denotes the sum of the square deviation, which reflects the differences in the experimental results due to the change at every level of each factor. Furthermore, df denotes the degree of freedom of the factor, which is equal to three in the present study; MS denotes the variance and can be calculated as $MS = SS/df$; F denotes the value for inspection, which indicates the degree of influence of the factor.

The critical value $F_{0.01}$ (3, 6) for the inspection level (0.01) can be determined in the distribution table of F-value, which is 9.78. Comparing the F value of each factor with the critical value $F_{0.01}$ (3, 6), R and $θ$ are determined as the prominent impact factors on the driving force of SMPC booms, which are marked as '***' and '**' based on the order of importance. Conversely, t has a limited influence on the driving force.

5 Design, Manufacture, and Experiment of Reel-Type Solar Array

5.1 Mechanism Design

For most existing flexible solar arrays, deployment is realized via motors or elastic strain energy stored in the boom [3–8]. In this study, we proposed a novel
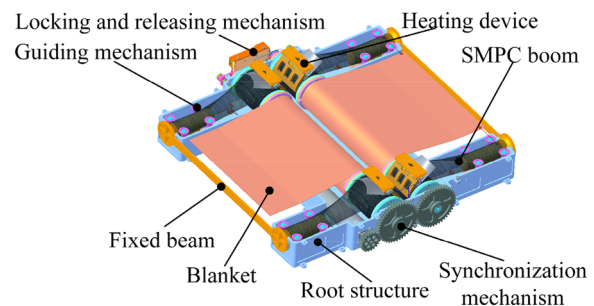
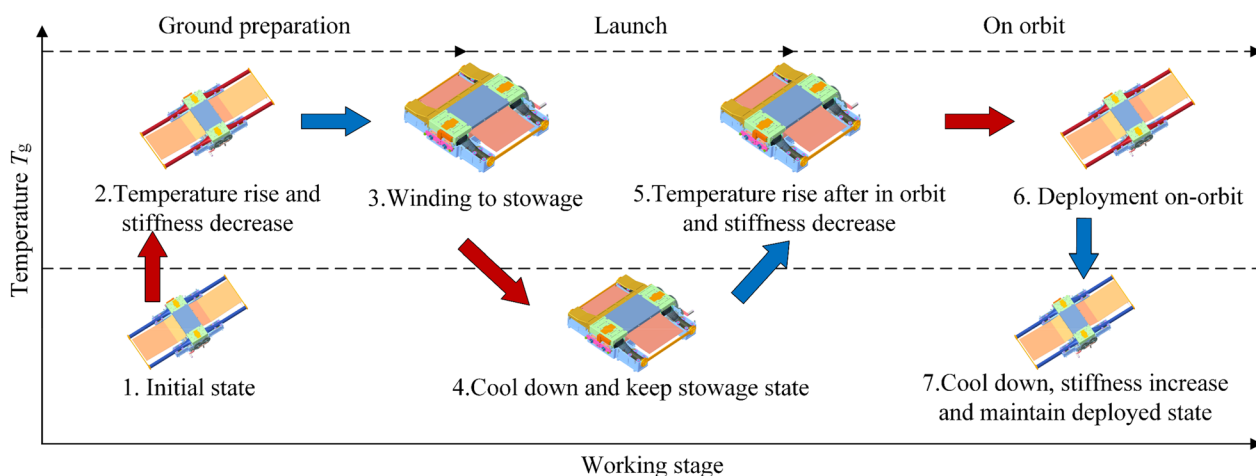**Figure 17** Model of reel-type solar array in stowed configuration (the upper cover is hidden)

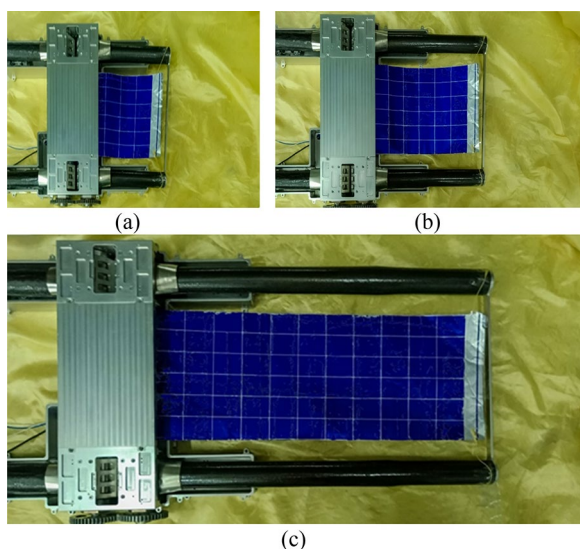**Figure 18** Principles of storage and deployment of the reel-type solar array

Figure 19 Deployment process of the reel-type solar array: **a** Stowed state, **b** Partially deployed, **c** Fully deployed

reel-type solar array driven by the self-deployment of the SMPC boom, which differs significantly from traditional approaches. A reel-type solar array with stowed configuration is shown in Figure 17. The reel-type solar array consisted of two flexible solar wings, and each wing comprised heating devices, guide mechanisms, fixed beams, blankets, synchronization mechanisms, and two SMPC booms [30].

Figure 18 illustrates the operation of the reel-type solar array. First, the temperature is raised above T_g to soften the SMPC boom. Then, the circular ring cross-section is flattened, and the SMPC boom is rolled into the mandrel. Subsequently, the boom cools down, storing the solar array in its entirety for launch. After the satellite is

in orbit, the locking and releasing mechanism is released, and the SMPC booms are heated again, and they return to their initial deployed state, rolling the blanket outward under the action of the guiding mechanism. By the time the SMPC booms are fully deployed, the temperature decreases below T_g, and the SMPC changes to a glass state, thereby improving the structural stiffness of the booms. Finally, the reel-type solar array operates with high-stiffness SMPC booms to satisfy the operating requirements.

5.2 Deployment Demonstration

To verify the feasibility of the deployment scheme of the reel-type solar array, a simplified prototype was developed in this study (only a single solar wing with two SMPC booms was manufactured). As mentioned above, the SMPC boom is the core component of the solar array and can realize self-deployment owing to its shape-memory characteristics. The properties of the SMPC boom can be used to determine the performance of the entire mechanism, whose parameters in this experiment are as follows: length of 500 mm, radius of 24 mm, thickness of 1 mm, and opening angle of 120°.

The experimental procedure was as follows. First, a heating chamber was used to heat the SMPC boom until it softened. One end of the boom is flattened and rolled into the mandrel. Second, a resistor heater is attached to the surface of the heating device. Then, the heating device, mandrel, and other parts of the mechanism are assembled together. The simplified reel-type solar array in stowed configuration is shown in Figure 19(a). Third, a current of 0.2 A is applied to both resistor heaters simultaneously. The resistor heater heats the SMPC boom, and the boom begins to recover its initial deployed shape

Xiao *et al. Chinese Journal of Mechanical Engineering*   (2023) 36:67

Page 12 of 13

automatically, rolling the blanket out simultaneously. The deployment process is illustrated in Figure 19. During the first 20 s of the deployment process, the displacement of the SMPC boom was almost zero because the resistor heater preheated the boom at this time. When the temperature increased above T_g, the SMPC boom began to recover, unrolling at a velocity of approximately 1 mm/s. The entire deployment process was smooth and stable, proving that the SMPC boom can be used as a deployable unit to drive the flexible solar array.

6 Conclusions

In this study, a flexible reel-type solar array that can realize self-deployment without complex driving and control mechanisms was introduced. The primary component of the solar array was the SMPC boom, which can be heated to recover its original shape, and thereby, enabling it to roll out the solar-cell blanket. The mechanical performance of the SMPC boom, such as its bending and buckling behavior, was critical to the performance of the solar array. These characteristics can be determined by the geometric parameters of the boom such as radius, thickness, opening angle, and length. The SMPC boom exhibited shape memory characteristics when heated and can deploy 100 mm within 75 s at specific geometric parameters. The recovery force of the SMPC boom is closely correlated with its radius and opening angle; however, the thickness of the laminate is less influential. The prototype of the reel-type solar array can self-deploy successfully, and the deployment velocity was approximately 1 mm/s. This study constitutes one of the explorations of SMPC booms in reel-type solar arrays. The results of the study can provide a reference for future research and development of flexible solar arrays. In future studies, the potential applications of SMPC booms in space-deployable structures should be considered.

Author contributions
HX and SW was in charge of the whole trial; DX wrote the manuscript; RL and HG revised the manuscript; LM and YW assisted with sampling and laboratory analyses. All authors read and approved the final manuscript.

Authors' Information
Hong Xiao, born in 1988, is currently a PhD candidate at *Research Center of Aerospace Mechanism and Control (RCAMC), Harbin Institute of Technology, China*. His research interests include aerospace deployable mechanism.
Sijie Wu, born in 1996, is currently an engineer at *Yinhe Hangtian Internet Technology Co. Ltd, China*. His research interests include solar array mechanism.
Dongdong Xie, born in 1997, is currently a master student at *RCAMC Harbin Institute of Technology, China*. His research interests include aerospace deployable mechanism.

Availability of Data and Materials
Not applicable.

Declarations

Ethics Approval and Consent to Participate
Not applicable.

Consent for Publication
Not applicable.

Competing Interests
The authors declare no competing financial interests.

References
[1] P A Jones, B R Spence. Spacecraft solar array technology trends. *IEEE Aerospace and Electronic Systems Magazine*, 2011, 26(8): 17-28.
[2] J Gibb, S Billets. A case study: Integrating triple-junction solar cells into flat-folding flexible solar array panels. *35th IEEE Photovoltaic Specialists Conference*, Honolulu, USA, June 20-25, 2010: 000731-000735.
[3] B Hoang, S White, B Spence, et al. Commercialization of deployable space systems' roll-out solar array (ROSA) technology for space systems Loral (SSL) solar arrays. *IEEE Aerospace Conference*, Big Sky, USA, March 5-12, 2016, 1-12.
[4] L Gerlach, A Fournier-Sicre, A Fromberg, et al. Hubble space telescope solar generator design for a decade in orbit. *IEEE Conference on Photovoltaic Specialists*, Kissimmee, USA, May 21-25, 1990: 1308-1313.
[5] C L Foster, M L Tinker, G S Nurre, et al. Solar-array-induced disturbance of the Hubble space telescope pointing system. *Journal of Spacecraft and Rockets*, 1995, 32(4): 634-644.
[6] B R Spence, S F White. Directionally controlled elastically deployable roll-out solar array: US, 8683755. 2014-4-1[2020-6-1]. https://patents.google.com/patent/US8683755.
[7] B R Spence, S White, M LaPointe, et al. International space station (ISS) roll-out solar array (ROSA) spaceflight experiment mission and results. *7th World Conference on Photovoltaic Energy Conversion (WCPEC)(a Joint Conference of 45th IEEE PVSC, 28th PVSEC and 34th EU PVSEC)*, Waikoloa, USA, June 10-15, 2018: 3522-3529.
[8] J Banik, S Kiefer, M LaPointe, et al. On-orbit validation of the roll-out solar array. *2018 IEEE Aerospace Conference*, Big Sky, USA, March 3-10, 2018: 1-9.
[9] J N Ran, P T Han, Z Z Cao, et al. Overview of thin-walled tubular space deployable masts. *Mechanics*, 2019, 46(10): 44-51. (in Chinese)
[10] A Lendlein, S Kelch. Shape-memory polymers. *Angewandte Chemie International Edition*, 2002, 41(12): 2034-2057.
[11] D Ratna, J Karger-Kocsis. Recent advances in shape memory polymers and composites: A review. *Journal of Materials Science*, 2008, 43(1): 254-269.
[12] I S Gunes, S C Jana. Shape memory polymers and their nanocomposites: A review of science and technology of new multifunctional materials. *Journal of Nanoscience and Nanotechnology*, 2008, 8(4): 1616-1637.
[13] T N Ren, G M Zhu, J Nie. Research progress on deployable structures of shape memory polymer composites. *Journal of Aeronautical Materials*, 2018, 38(4): 47-55.
[14] L W Liu, W Zhao, X Lan, et al. Soft intelligent material and its applications in aero-space. *Journal of Harbin Institute of Technology*, 2016, 48(5): 1-17. (in Chinese)
[15] J S Leng, X Lan, Y J Liu, et al. Shape memory polymers composites and their applications in deployable structures. *Journal of Astronautics*, 2010, 31(4): 950-956.

[16] D Zhang, Y J Liu, J S Leng. Fiber reinforced shape memory polymer composites and their applications in aerospace. *Acta Materiae Compositae Sinica*, 2021, 38(3): 698-711. (in Chinese)

[17] P D Yu, X H Guan, D D Wang et al. Preparation and properties of novel optical and thermal dual response shape memory polymers. *Chemical Journal of Chinese Universities*, 2022, 43(6): 290-298. (in Chinese)

[18] J S Leng, W M Huang, X Lan et al. Significantly reducing electrical resistivity by forming conductive Ni chains in a polyurethane shape-memory polymer/carbon-black composite. *Applied Physics Letters*, 2008, 92(20): 204101.

[19] Y Liu, Y Guo, J Zhao et al. Carbon fiber reinforced shape memory epoxy composites with superior mechanical performances. *Composites Science and Technology*, 2019, 177: 49-56.

[20] R Barrett, W Francis, E Abrahamson et al. Qualification of elastic memory composite hinges for spaceflight applications. *47th AIAA/ASME/ASCE/AHS/ASC Structures, Structural Dynamics, and Materials Conference*, Rhode Island, Newport, May 1-4, 2006: 2039.

[21] H Zhao, X Lan, L Liu et al. Design and analysis of shockless smart releasing device based on shape memory polymer composites. *Composite Structures*, 2019, 223: 110958.

[22] F Li, L Liu, X Lan et al. Preliminary design and analysis of a cubic deployable support structure based on shape memory polymer composite. *International Journal of Smart and Nano Materials*, 2016, 7(2): 106-118.

[23] F Li, L Liu, L Du, et al. Mechanical analysis of a tip-loaded deployable truss based on shape memory polymer composite. *Composite Structures*, 2020, 242: 112196.

[24] G L Shen, G K Hu. *Mechanics of composites (2nd edition)*. Beijing: Tsinghua University Press, 2013. (in Chinese)

[25] ASTM D3039/D3039M-17 Standard Test Method for Tensile Properties of Polymer Matrix Composite Materials, 2017. https://www.astm.org/d3039_d3039m-17.html.

[26] ASTM D5379/D5379M-19e1 Standard Test Method for Shear Properties of Composite Materials by the V-Notched Beam Method, 2021. https://www.astm.org/d5379_d5379m-19e01.html.

[27] ASTM D3518/D3518M-18 Standard Test Method for In-Plane Shear Response of Polymer Matrix Composite Materials by Tensile Test of a$\pm$45 Laminate, 2018. https://www.astm.org/d3518_d3518m-18.html.

[28] F Shadmehri, B Derisi, S V Hoa. On bending stiffness of composite tubes. *Composite Structures*, 2011, 93(9): 2173-2179.

[29] W He, W D Xue, B Tang. *Optimization design method and data analysis*. Beijing: Chemical Industry Press, 2012. (in Chinese)

[30] H W Guo, Z Q Deng, R Q Liu, et al. A repeated spreading and retracting mechanism of elastic extension boom of flexible solar wing: CN, 109094821. 2018-12-28[2020-6-30]. (in Chinese).